Widespread occurrences of variably crystalline ^{13}C-depleted graphitic carbon in banded iron formations

Matthew S. Dodd [a,b,c], Dominic Papineau [a,b,c,d], Zhen-Bing She [d], Chakravadhanula Manikyamba [e], Yu-Sheng Wan [f], Jonathan O'Neil [g], Juha A. Karhu [h], Hanika Rizo [i], Franco Pirajno [j]

[a] London Centre for Nanotechnology, University College London, WC1H 0AH, UK
[b] Department of Earth Sciences, University College London, WC1E 6BT, UK
[c] Centre for Planetary Sciences, University College London, WC1E 6BT, UK
[d] School of Earth Sciences & State Key Laboratory of Biogeology and Environmental Geology, China University of Geosciences, Wuhan, China
[e] National Geophysical Research Institute, Hyderabad, India
[f] Beijing SHRIMP Centre, Institute of Geology, Chinese Academy of Geological Sciences, China
[g] Ottawa-Carleton Geoscience Centre, Department of Earth and Environmental Sciences, University of Ottawa, Ottawa, K1N 6N5, Canada
[h] Department of Geosciences and Geography, University of Helsinki, P.O. Box 64, Finland
[i] Ottawa-Carleton Geoscience Centre, Department of Earth Sciences, Carleton University, Ottawa, K1S 5B6, Canada
[j] Centre for Exploration Targeting, The University of Western Australia, 35 Stirling Highway, Crawley, WA 6009, Australia

ARTICLE INFO

ABSTRACT

Almost all evidence for the oldest traces of life on Earth rely on particles of graphitic carbon preserved in rocks of sedimentary protolith. Yet, the source of carbon in such ancient graphite is debated, as it could possibly be non-biological and/or non-indigenous in origin. Here we describe the co-occurrence of poorly crystalline and crystalline varieties of graphitic carbon with apatite in ten different and variably metamorphosed banded iron formations (BIF) ranging in age from 1,800 to >3,800 Myr. In Neoarchean to Palaeoproterozoic BIF subjected to low-grade metamorphism, ^{13}C-depleted graphitic carbon occurs as inclusions in apatite, and carbonate and arguably represents the remineralisation of syngenetic biomass. In BIF subjected to high-grade metamorphism, ^{13}C-depleted graphite co-occurs with poorly crystalline graphite (PCG), as well as apatite, carbonate, pyrite, amphibole and greenalite. Retrograde minerals such as greenalite, and veins cross-cutting magnetite layers contain PCG. Crystalline graphite can occur with apatite and orthopyroxene, and sometimes it has PCG coatings. Crystalline graphite is interpreted to represent the metamorphosed product of syngenetic organic carbon deposited in BIF, while poorly crystalline graphite was precipitated from C–O–H fluids partially sourced from the syngenetic carbon, along with fluid-deposited apatite and carbonate. The isotopic signature of the graphitic carbon and the distribution of fluid-deposited graphite in highly metamorphosed BIF is consistent with carbon in the fluids being derived from the thermal cracking of syngenetic biomass deposited in BIF, but, extraneous sources of carbon cannot be ruled out as a source for PCG. The results here show that apatite + graphite is a common mineral assemblage in metamorphosed BIF. The mode of formation of this assemblage is, however, variable, which has important implications for the timing of life's emergence on Earth.

© 2019 Elsevier B.V. All rights reserved.

1. Introduction

The association of isotopically-light organic carbon and apatite is a common feature of sediments incorporating biomass (Papineau et al., 2016; She et al., 2014). Apatite [Ca$_5$(PO$_4$)$_3$(F, Cl, OH)] requires phosphorus, which can be derived from the decomposition of phosphorus-bearing biological organic matter (biomass) in sediments. This knowledge has been combined with observations of isotopically-light carbon in graphite in association with apatite, to argue for a biological origin of graphite (Mojzsis et al., 1996) in the ca. 3,830 million years old (Myr) Akilia quartz–pyroxene rock. Additionally, the presence of apatite rosettes (Li et al., 2012) and apatite with ferric acetate (Li et al., 2011) have been used to propose the biological processing of phosphorus and organic carbon in BIF. Alternatively, it has been suggested that graphite associated with apatite in metamorphosed BIF may also be fluid-deposited

(Lepland et al., 2011; Papineau et al., 2010a, 2011, 2010b), so that non-biological and biological sources of organic carbon are both possible. To assess how common associations of graphitic carbon and apatite are in BIF, as well as the origin of the carbon in graphite, we document its mineral associations in ten different samples of various ages and metamorphic grades. Selected samples come from the Eoarchaean supracrustal terranes of Nuvvuagittuq, Akilia, and Saglek, from the Neoarchean belts of Sandur, Temagami, Anshan, and Wutai, as well as from the Paleoproterozoic Brockman, Pääkkö, and Biwabik iron formations (Table 1; Fig. 1; Supplementary information).

2. Methods

2.1. Optical microscopy

Standard 30 μm thick, polished and doubly-polished thin sections were prepared with a final polishing step using Al_2O_3 0.5 μm powder for investigation using transmitted and reflected light microscopy. No immersion oil was used to map petrographic features in thin section.

2.2. Micro-Raman spectroscopy

Micro-Raman microscopy was conducted on petrographic targets within the polished thin sections using a WiTec alpha 300 confocal Raman imaging microscope with a 532 nm wavelength laser and operating at a power between 0.1 and 6 mW depending on the target. Raman spectra and hyperspectral scans were performed at 1000X magnification with variable spatial resolutions from 1 μm to 360 nm, and spectral resolutions of 4 cm^{-1} were achieved using a 600 lines/mm grating. Hyperspectral images were created for specific mineral phases using peak intensity mapping for characteristic peaks of each individual mineral in a scan. Average spectra were calculated by creating a mask on homogeneous pixels of individual phases and had their backgrounds fitted to a polynomial function and subtracted. Large area scans (>100 μm × 100 μm) were completed using the same process outlined previously, with spatial resolutions no lower than 1 μm. Peak parameters were calculated from a Lorenz function modelled for each selected peak. Cosmic ray reduction was applied to all Raman spectra. Raman spectra were collected at confocal depths of at least 1 μm below the surface of the thin sections. Raman spectrum parameters, such as peak positions, Full Width at Half Maximum (FWHM), and areas under the curve were extracted from the best-resolved Raman peaks, and modelled with Lorentz function on background-subtracted spectra. To estimate maximum crystallisation temperatures of graphitic carbon from the Raman spectra, we used the geothermometer of Beyssac et al. (2002), which is justified by the lower greenschist to granulite metamorphic grade of all the studied banded iron formations.

2.3. Scanning electron and energy dispersive X-ray spectroscopy

Scanning electron microscopy (SEM) in back scattered electron (BSE) and secondary electron (SE) imaging modes were used to characterise the morphology and composition of selected targets, which were also characterised by energy dispersive X-ray spectroscopy (EDS). Analyses were carried out in the Department of Earth Sciences at University College London (UCL) using a JEOL JSM-6480L SEM. Standard operating conditions for SEM imaging and EDS analysis were a 15 kV accelerating voltage, working distance of 10 mm and an electron beam current of 1 nA. Samples were always coated with a few nanometres of Au prior to analysis. The analyses were calibrated against standards of natural silicates, oxides and Specpure® metals, with the data corrected using a ZAF program.

2.4. Stable isotope mass spectrometry

Analyses of bulk rock powders for graphitic carbon were conducted in the Bloomsbury Environmental Isotope Facility at UCL with a Thermo-Finnigan Flash 1112 EA connected to a Thermo Delta V Isotope Ratio Mass Spectrometer via a Conflo IV gas distribution system. Sample preparation and analytical details follow a previously devised protocol (Dodd et al., 2018). A suite of standard materials that span a range of $\delta^{13}C$ values from $-26‰$ to $-6‰$, was analysed within each run. Each standard was analysed multiple times through the run to ensure reproducibility. The results were calibrated to the Vienna Pee Dee Belemnite (VPDB) scale with a reproducibility better than $0.2‰$ (1σ; $n = 19$). Empty muffled silver capsules were run with and without HCl added to test for contamination prior to analysis. No carbon was detected in these procedural blank silver capsules. Analyses of bulk rock powders for carbonate were conducted in the Cardiff School of Earth Sciences with a Thermo Finnigan Delta V Advantage mass spectrometer connected to a Gas Bench II. Sample preparation and analytical details follow a previously devised protocol (Dodd et al., 2018).

3. Results and discussion

3.1. Occurrences of graphitic carbon in highly metamorphosed BIF

Apatite in the amphibolite facies ca. 4,280-3,770 Myr Nuvvuagittuq silicate BIF (quartz + magnetite + Fe-silicates; Table 1; Fig. 1) appears with fluid inclusions of CO_2 + CH_4 + H_2O (Fig. 2) within quartz grains, along grain boundaries and with retrograde greenalite (Fig. 3a; Supplementary Table 1). In the Nuvvuagittuq jasper BIF (quartz + haematite + magnetite), apatite occurs as inclusions in calcite rosettes, chert + magnetite granules, and as millimetre-size graphite-bearing euhedral laths (Dodd et al., 2017). Notably for the Nuvvuagittuq silicate BIF, graphite co-occurs with poorly crystalline graphite (PCG) as coatings on apatite, which also hosts inclusions of magnetite, calcite and graphite (Fig. 3a–d). Poorly crystalline graphite has more intense Raman D peaks than G peaks, which yields D/G peak intensity ratios above 1, in contrast to crystalline graphite which has weak intensity D peaks compared to G peaks, giving intensity ratios below 1 (Fig. 4; Supplementary Fig. 1). These differences lead to estimates of crystallisation temperatures for PCG between 60–200 °C lower than those of graphite in the same sample (Fig. 4; Supplementary Table 2). In the Nuvvuagittuq silicate BIF, PCG appears within phyllosilicate masses of greenalite and minnesotaite, and occurs with accessory minerals such as carbonate and sulfide that are present in between coarse quartz crystals (Fig. 3e–g), which demonstrates a retrograde origin. Furthermore, PCG occurs within orthopyroxene crystals and coats calcite and retrograde hornblende inclusions (Fig. 3h–j; Supplementary Table 1). In other instances, PCG and graphite co-exist with calcite and magnetite inside orthopyroxene crystals (Fig. 5). Similarly, in the ca. 3,920 Myr old Saglek–Hebron silicate BIF (Table 1; Fig. 1), crystalline graphite appears inside apatite and as coatings on apatite (Fig. 3j–l), demonstrating that this is a common mineral association among Eoarchean BIF.

The ca. 2,551 Myr old, amphibolite facies Anshan BIF (Table 1; Fig. 1), also hosts inclusions of PCG associated with greenalite and apatite along with graphite. Graphite is also present within prograde grunerite crystals (Fig. 6a–b). Similarly, both graphite and PCG have been found in association with apatite and greenalite in carbonate, situated adjacent to magnetite–pyrite bands (Fig. 6c–d). In the ca. 2,500 Myr, greenschist facies Wutai BIF (Table 1; Fig. 1), apatite forms microscopic clusters within masses of ankerite present in pyrite-rich layers, in which graphite co-occurs within microns of PCG, apatite and feldspar (Fig. 6e–f). In the ca. 1,878 Myr hornfels–pyroxene facies Biwabik BIF (Table 1; Fig. 1), graphite

Table 1
Summarised details of the BIF samples included in this study. See supplementary information for detailed review of the samples.

Banded iron formation	Location	Age (Myr)	Metamorphic facies	Associated lithologies	Mineralogy of iron formation
Saglek	N58 23 53.13 W63 6 41.85	3, 7803–3, 920	Amphibolite	Mafic volcanics, pelitic rocks, carbonate rocks, conglomerate, chert, ultramafic rocks	Qtz-mag-pyx-apa
Akilia	N63 55 40 W51 41 30	>3,830	Granulite	Mafic amphibolite and ultramafic rocks, leucogranite, quartzofeldspathic orthogniess	Qtz-pyx-hbl-sulphides-cal-apa-gra
Nuvvuagittuq	PC0802 – N58 16 43.5 W77 43 57.7 PC0810 – N58 18 07.4 W77 43 51.2 PC0814 – N58 17 12.3 W77 44 11.6 PC0825 – N58 17 08.7 W77 44 12.2 PC-014 – N58 17 50.22 W77 44 10.09 PC-075 – 58 17 33.4 W77 44 2.34 PC-091 N58 17 31.57 W77 44 6.44	4,280–3,770	Amphibolite	Amphibolite, orthogniess, chlorite meta-volcanics, serpentinite, ultra-mafics, quartz-biotite schist, fuschite silica formation, conglomerate	Qtz-mag-pyx-gru-gre-apa-gra
Sandur	N 15 06 19 W 76 34 50	Ca. 2,700	Greenschist	Carbon shales, mafic and felsic volcanics, greywacke	Qtz-mag-sd-py-silicates-apa-gra
Temagami	Sherman mine, Ontario	Ca. 2,700	Greenschist	Mafic volcanics and turbidites	Qtz-mag-ank-mns-apa-gra
Anshan	Drill core taken several kilometres south east of Qidashan, Liaoning province	Ca. 2,550	Amphibolite	Metavolcanic amphibolite, finegrained biotite gneiss, quartzite, phyllite and schists	Qtz-mag-gru-ank-gre-py-apa-gra
Wutai – Baizhiyan fm.	Puhsang mine, Shanxi province	Ca. 2,500	Greenschist	Chlorite–actinolite schist, intermediate-felsic volcanics	Qtz-mag-ank-py-chm-apa-gra
Dales Gorge	DGH-1 drill core	Ca. 2,500	Lower greenschist	Black shale and chert	Qtz-mag-sd-mns-stp-hem-apa-gra
Pääkkö	Drill core #344 – M – 52/3441/73/344	1,920–2,000	Low amphibolite	Dolomites-black shale, phyllite, metadiabase, quartzite	Qtz-mag-py-gru-ab-gra
Biwabik	47.68 N 91.88 W	Ca. 1,880	Granulite	Quartzite	Qtz-pyx-mag-gru-gra

Mineral abbreviations: Qtz – quartz, mag – magnetite, py – pyrite, pyx – pyroxene, gru – grunerite, gra – graphite, apa – apatite, stp – stilpnomelane, hem – haematite, sd – siderite, mns – minnesotaite, chm – chamosite, gre – greenalite, ank – ankerite, hbl – hornblende, cal – calcite, ab – albite

occurs with calcite within retrograde grunerite, as evidenced by grunerite appearing as rims along the margins of orthopyroxene (Fig. 6g–h). Similarly in the ca. 3,830 Myr old granulite facies Akilia quartz–pyroxene rock (Table 1; Fig. 1), graphite also occurs within retrograde grunerite rims along the margins of orthopyroxene crystals, occasionally associated with chalcopyrite (Papineau et al., 2010a) (Supplementary Fig. 2). In contrast, abundant graphite is found in discrete layers of prograde grunerite, pyrite, feldspar, and magnetite with apatite (Fig. 6h–j) in the ca. 2,000 Myr old, lower amphibolite facies Pääkkö BIF (Table 1; Fig. 1).

3.2. Occurrences of graphitic carbon in BIF metamorphosed to the greenschist facies

Graphitic carbon was also mapped by micro-Raman in the greenschist facies Dales Gorge, Temagami and Sandur BIF (Table 1; Fig. 1). In the ca. 2,470 Myr Dales Gorge BIF (Table 1; Fig. 1), apatite can form variably thick bands varying up to 600 μm in thickness. These bands are associated with stilpnomelane or minnesotaite and siderite/ankerite between magnetite layers. The apatite contains numerous inclusions of microscopic haematite, ankerite, graphitic carbon and pyrite (Fig. 7a–b). The graphitic carbon tends to form discrete layers in the apatite and cluster around ankerite inclusions within the apatite (Fig. 7b). Graphitic carbon is preferentially preserved within the apatite, with minor amounts in the surrounding quartz and ankerite (Fig. 7b). In the ca. 2,736 Myr Temagami BIF (Table 1; Fig. 1), there are magnetite and minnesotaite bands interlayered with apatite bands, which are nearly one millimetre thick, with inclusions of ankerite and graphitic carbon (Fig. 7c–d). In contrast to the Dales Gorge BIF, the Temagami graphitic carbon occurs predominately in ankerite inclusions within millimetre thick apatite bands (Fig. 7d). The ca. 2,700

Myr Sandur BIF (Table 1; Fig. 1) preserves a range of graphitic carbon crystallinities (Fig. 7e–g; 4) including graphite and PCG, which occur with apatite, siderite and pyrite. Hence, these observations show for the first time that graphite and PCG co-occur in BIF, and that they are also commonly associated with apatite and carbonate.

### 3.3. Syngenicity of graphitic carbon

Graphitic carbon may be damaged during polishing of petrographic thin sections, but can be distinguished by enlarged D peaks in the Raman spectra (Beyssac et al., 2003). Therefore, it has been verified through optical microscopy that all PCG targets are found below the thin section surface and were not modified by polishing. In addition, orientation of graphite sheets relative to the Raman laser may induce changes in the relative intensities of the D peak (Wang et al., 1989). Yet, graphite sheet orientation creates relatively minor changes in D peak intensities and could not account for the large difference in intensities of D to G peaks observed here between PCG and graphite (Supplementary Fig. 1 and Supplementary Table 2). The crystalline structural differences between PCG and graphite are therefore a result of their mode of formation, and the two types can be clearly distinguished by Raman crystallographic characteristics (Supplementary Fig. 1).

The crystallisation temperature estimates for PCG are interpreted as retrograde crystallization temperatures of fluid-deposited graphite, although we stress these may not be accurate, as the graphite-Raman thermometer was calibrated against prograde mineral assemblages (Beyssac et al., 2002) (Supplementary Table 2). A better judge of precipitation temperatures can be discerned from the occurrence of PCG with retrograde minerals like
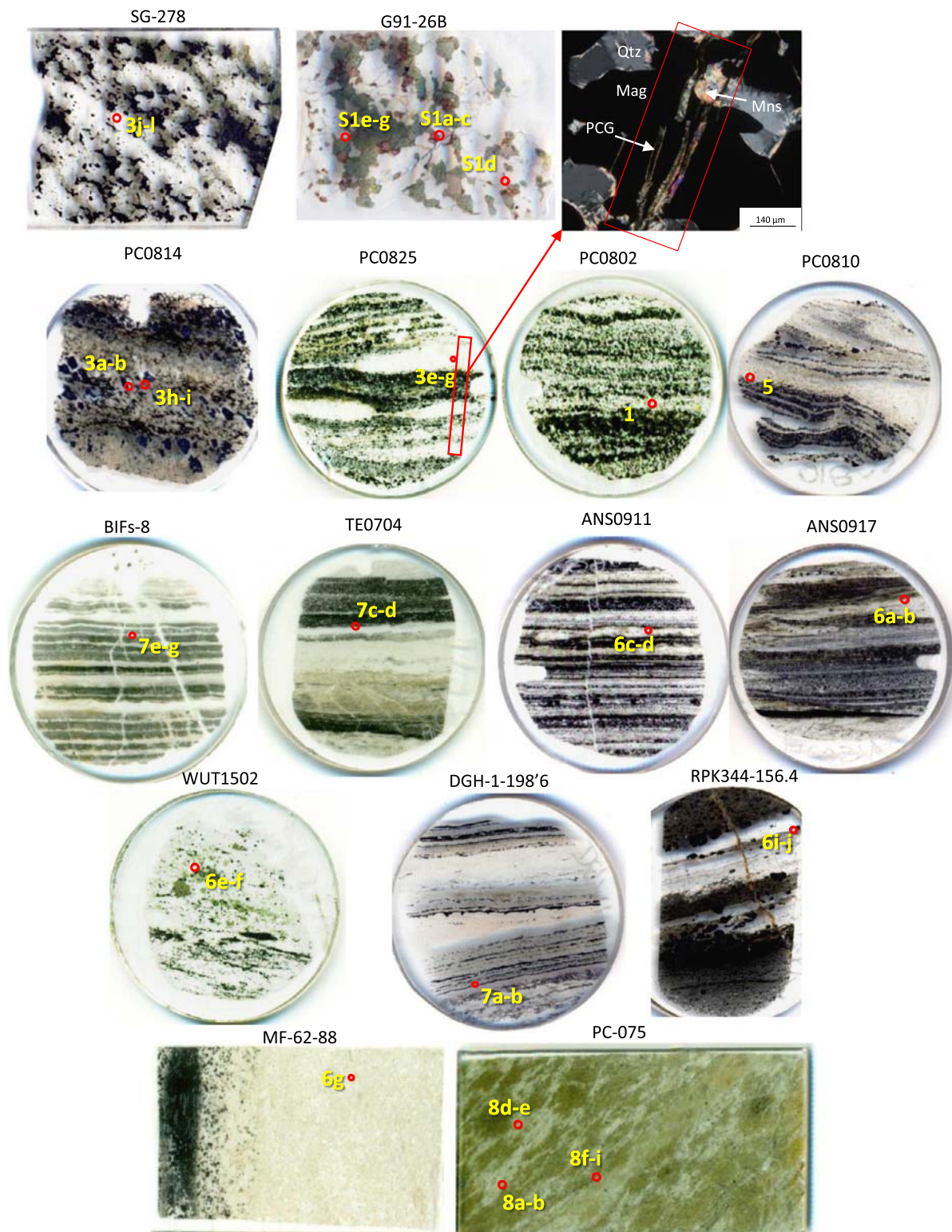
Fig. 1. Thin section scans of samples in this study. SG-278 – Saglek BIF. G91-26B – Akilia quartz–pyroxene rock. PC0814, PC0825 (red box = graphite vein), CP image of poorly crystalline graphite and minnesotaite vein cutting magnetite bands. PC0802, PC0810 – Nuvvuagittuq BIF. ANS0911, ANS0917 – Anshan BIF. WUT1502 – Wutai BIF. BIFs-8 – Sandur BIF. DGM-1-198'6 – Brockman, Dales Gorge BIF. TE0704 – Temagami. RPK344-156.4 – Pääkkö. MF-62-88 – Mesabi BIF. PC-075 – Nuvvuagittuq serpentinite. All round sections are 2.5 cm in diameter. Rectangle section are 2.5 cm wide. (For interpretation of the colours in the figure(s), the reader is referred to the web version of this article.)
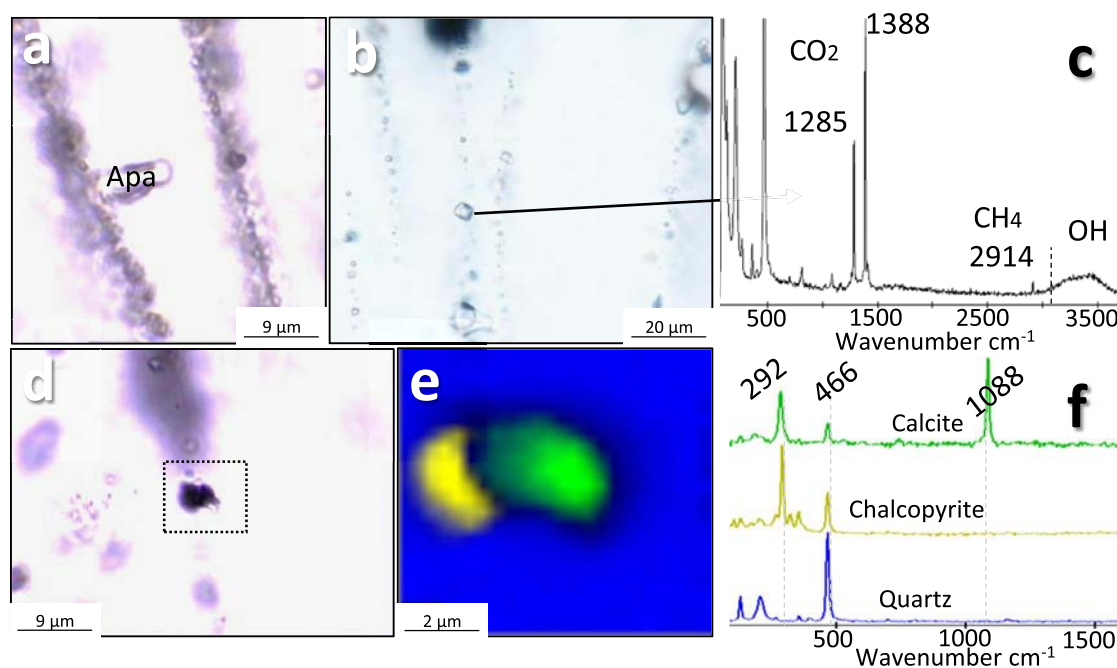
Fig. 2. Fluid inclusions in the Nuvvuagittuq BIF, PC0802. a) Transmitted light image of apatite with fluid inclusion trails. b) CO_2–CH_4–H_2O bearing fluid inclusions. c) Raman spectrum of fluid inclusion in b. d) Transmitted light image of calcite and chalcopyrite with fluid inclusion trail. e) Raman map showing calcite with chalcopyrite in fluid inclusion trail. f) Raman spectra for Raman map in e. Apa – apatite. Raman map colours: green – calcite, yellow – chalcopyrite, blue – quartz.
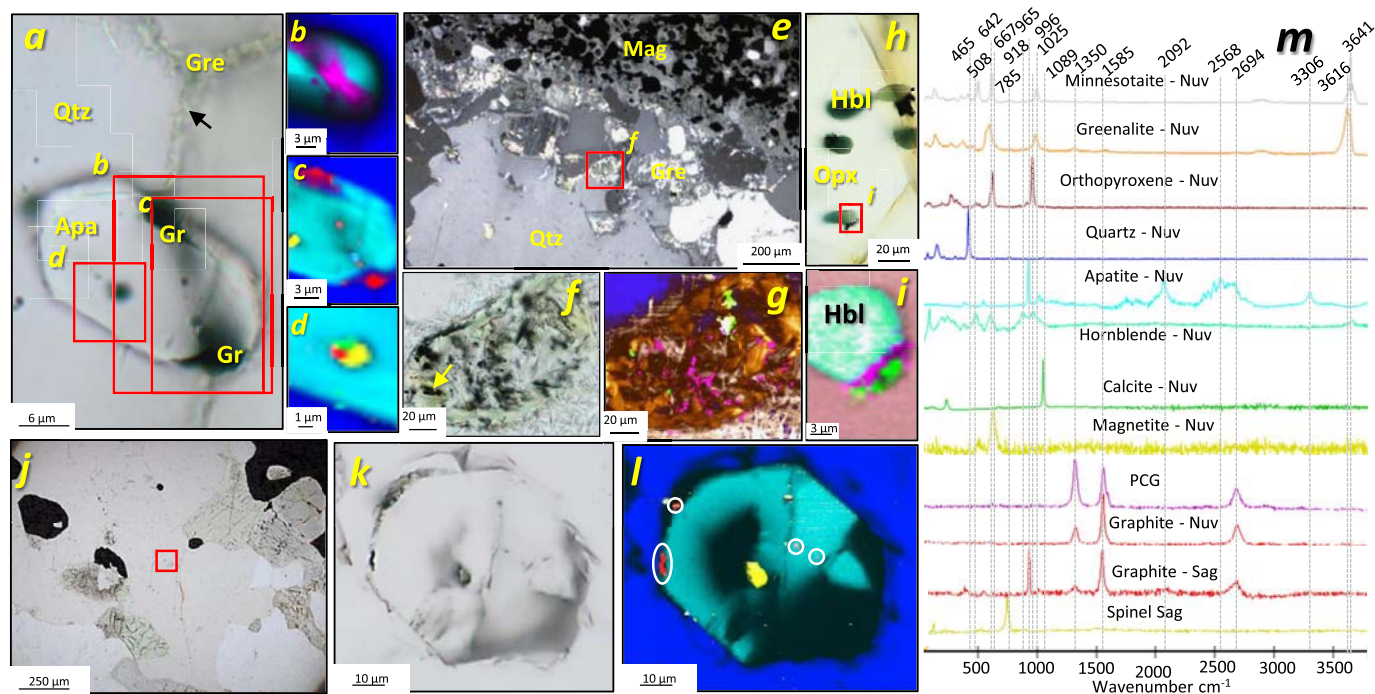
Fig. 3. Graphitic carbon associations in the Eoarchean–Hadean Nuvvuagittuq and Saglek BIF. a) Plane Polarised Light (PPL) image of apatite associated with multiple crystallinities of graphitic carbon, arrow points to greenalite filling cracks. b) Raman map of boxed area in panel b taken at a confocal depth of 5 μm. c–d) Raman maps of boxed areas in *a* at surface of thin section. e) Cross Polars (CP) image of greenalite between quartz grains. f) PPL image of greenalite cluster surrounded by minnesotaite (arrow points to sulfide grain). g) Raman map showing PCG associated with calcite inside the greenalite cluster. h) PPL image of orthopyroxene with inclusions of ferro-hornblende i) Raman map of PCG and calcite coating hornblende. j) PPL image of apatite location in the Saglek BIF, red box corresponds to panel k. k) PPL image of apatite with opaque inclusions and coatings. l) Raman image of panel k, showing graphite within and on the edges of the apatite grain (white circles), including an inclusion of spinel. m) Raman spectra for this figure. Mineral abbreviations: Apa – apatite, Gr – graphite, Gre – greenalite, Qtz – quartz, Mag – magnetite, Hbl – hornblende, Opx – orthopyroxene. Raman map colours: grey – minnesotaite, orange – greenalite, brown, orthopyroxene, blue – quartz, turquoise – apatite, light green – hornblende, green – calcite, yellow – magnetite (spinel – Saglek sample), purple – poorly crystalline graphite, red – crystalline graphite.
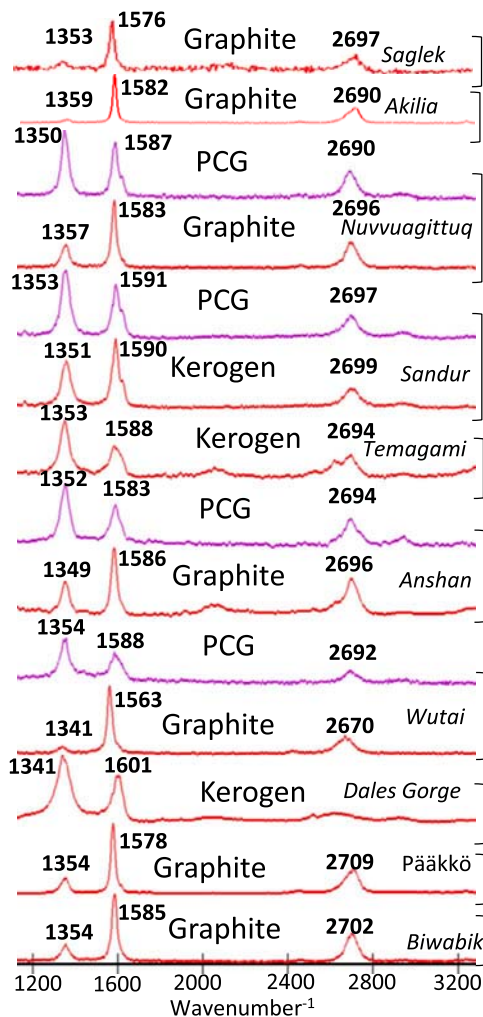
Fig. 4. Crystallinities of graphitic carbon in Archean and Palaeoproterozoic BIFs in order or decreasing age. Purple colour corresponds to poorly crystalline graphite (PCG) co-occurring with graphite. PCG is defined as having an intense D-peak (∼1350 cm^{-1}) relative to the G-peak (∼1580 cm^{-1}) and is distinguished from kerogen by the presence of a sharp 2D peak (∼2700 cm^{-1}).

minnesotaite (Fig. 3f–I; 6a–d, g), which has an upper stability limit of 350 °C (Klein, 2005), similar to the crystallisation temperatures calculated for PCG (Supplementary Table 2). This indicates that PCG was deposited from low temperature fluids during retrograde metamorphism in the Nuvvuagittuq, Anshan and Wutai BIF, supported by PCG appearing within veins cross-cutting sedimentary layers in the Nuvvuagittuq BIF (Fig. 1). However, retrograde minerals hosting graphitic carbon have not yet been found in the Wutai BIF. In the case of the granulite facies Biwabik BIF and Akilia quartz–pyroxene rock, graphite is associated with retrograde grunerite rims on prograde orthopyroxene crystals (Fig. 6g; Supplementary Fig. 2), depicting high temperature retrogression with carbonic fluids. However, the Dales Gorge, Temagami and Pääkkö BIF do not show evidence for retrogression, and preserve primary organo-mineral assemblages, indicative of metamorphosed, decayed biomass, such as ^{13}C-depleted kerogen inclusions in apatite and ^{13}C-depleted carbonate (Fig. 7a–d; Table 2). Crystallisation temperature estimates for graphite in the Sandur BIF exceeds metamorphic temperatures experienced by the formation (Supplementary Table 2), and therefore may be a result of non-metamorphic processes, such as templated mineral growth along quartz boundaries (Fig. 7g) (van Zuilen et al., 2012).

The retrograde phases in the Nuvvuagittuq, Anshan, Biwabik and Akilia are hydrated phyllosilicates and double-chained inosilicates (Fig. 3g–j; 6d, g–h, Supplementary Fig. 2). This points to cooling and hydration reactions as the precipitation mechanism of PCG (Luque et al., 2014). This can happen during cooling of C–O–H fluids and can lead to coinciding hydration of the host minerals and decreased carbon solubility, so that PCG precipitates (cf. Equ. (1)). In amphibolite facies BIF, amphiboles such as grunerite are prograde minerals, whereas in granulite facies BIF grunerite rims on pyroxene are more likely retrograde after pyroxene (Klein, 2005). Greenalite and minnesotaite would not survive amphibolite facies metamorphism and therefore they are also retrograde minerals (Klein, 2005).

$$CO_2 + CH_4 \rightarrow 2C + 2H_2O \qquad (1)$$

Significantly, the association of apatite with fluid inclusion trails in the Nuvvuagittuq BIF (Fig. 2) shows that fluids contained CO_2, CH_4, H_2O, H_2S, PO_4^{3-}, Ca^{2+}, Fe^{2+} and Cu^{2+} (Papineau et al., 2011), as indicated by the occurrence of chalcopyrite, calcite, apatite, and Fe^{2+}-bearing silicates along with fluid inclusions (Fig. 1). In the Akilia quartz–pyroxene rock, metamorphic apatite has been reported to contain carbonate, which could have been a source of carbon in graphite (Nutman and Friend, 2006). Graphite coatings on apatite in the Akilia quartz–pyroxene rock (Papineau et al., 2010a) co-occur in fluid inclusion trails containing $CO_2 + CH_4 + H_2O$ (Lepland et al., 2011), as well as sulphides and carbonate (Supplementary Fig. 2), which point to fluid-deposition from fluids compositionally-similar to those in the Nuvvuagittuq BIF. An important observation in the Nuvvuagittuq BIF, is that minnesotaite and greenalite are the dominant phyllosilicate minerals associated with PCG, which suggests that the metamorphic fluids were largely derived from within the BIF because these phases are common in BIF. Should the metamorphic fluids have been sourced from non-BIF lithologies, they would carry elevated concentrations of elements atypical for BIF, such as Ti or Al. Thus the absence of Al-phyllosilicates with PCG is consistent with the fluids being derived mainly from BIF elements (Fig. 3f–g) (Gaillard et al., 2018). The association of PCG and apatite can be explained by hydroxyapatite and phyllosilicates co-precipitating from fluids. These minerals would consume H_2O during precipitation reactions yielding PCG and H_2O through Equation (1). This precipitation of apatite is analogous to the dissolution and recrystallisation of graphite and carbonate-bearing apatite from granulite facies pelitic rocks of Cooma, South-East Australia (Nutman, 2007). Such processes can result in the observed association of apatite and graphitic carbons during retrograde reactions. In general, carbonate appears as microscopic crystals intimately associated with fluid-deposited carbon, probably as a result of increasing CO_2 disassociation in metamorphic fluids during cooling (Fig. 2; 3d, g, I; 6g).

3.4. Origins of poorly crystalline and crystalline graphitic carbon

PCG and graphite co-occur within micrometre distances in the Nuvvuagittuq, Anshan, and Wutai BIF (Fig. 3b–d; 5b–h; 6a–f). From the intimate association of these graphitic carbon phases, it can be inferred that they bear the same source and were transported together by similar metamorphic fluids. This is supported by PCG commonly found around, or coating, crystalline graphite in these BIF (Fig. 3a–d; 5d–h; 6d, f). This implies that the PCG grew on pre-existing crystalline graphite. Similar examples have been found in Proterozoic gneiss and quartzite from the Iberian metamorphic belt of Spain, where fluid-deposited graphite forms overgrowths on syngenetic graphite in gneiss and quartzite (Crespo et al., 2004), as well as in numerous other formations (Arita and Wada, 1990; Satish-Kumar et al., 2011; Valley and O'Neil, 1981). In addition,
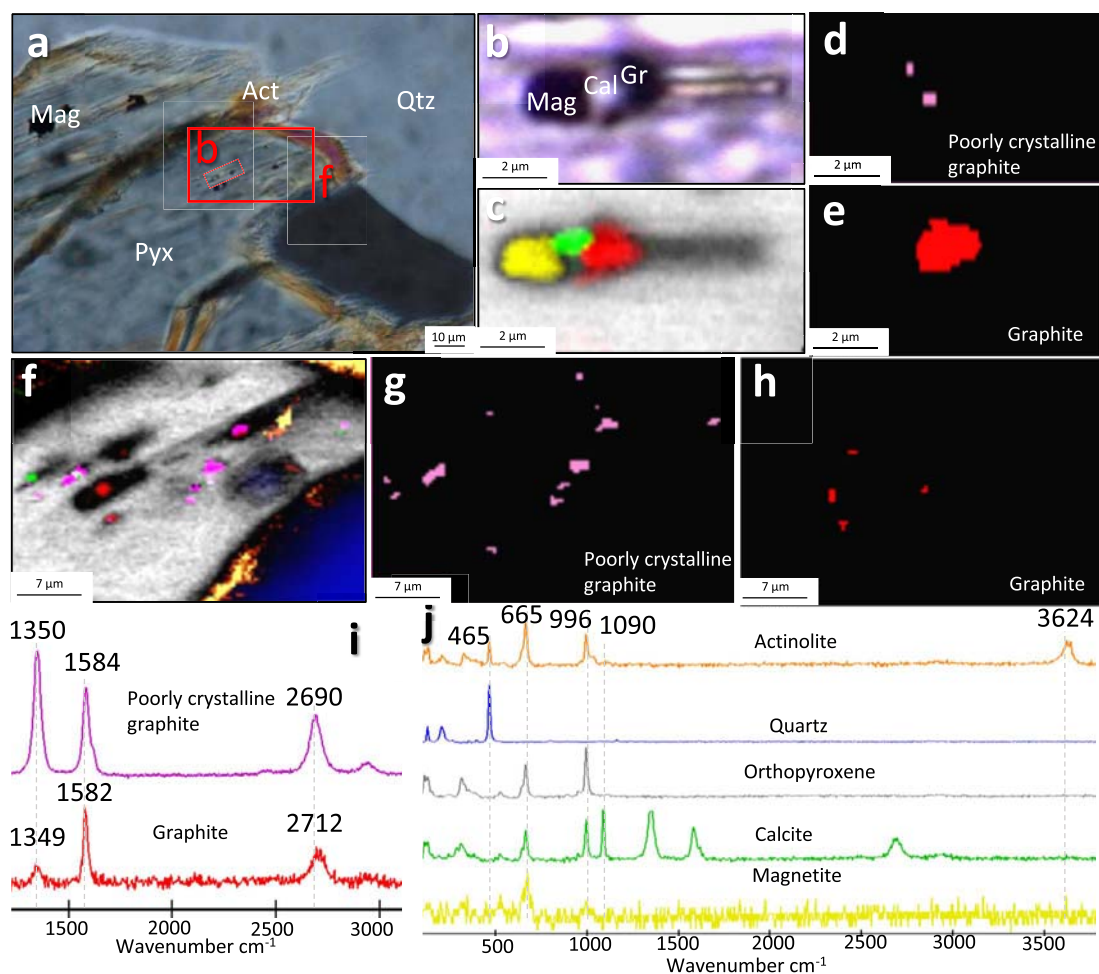
Fig. 5. Crystalline and poorly crystalline graphite in the Nuvvuagittuq BIF, PC0810. a) Cross polar image of pyroxene with serpentinised edges (orange); red boxes mark Raman maps. b) Transmitted light image of magnetite, carbonate and graphitic carbon in pyroxene. c) Raman map of magnetite, calcite and graphitic carbon in orthopyroxene. d–e) Raman filter map showing the intimate association of graphite and PCG. f) Raman map showing PCG, graphite and calcite in orthopyroxene. g–h) Raman filter map showing the close spatial association of PCG and graphite in f. i) Raman spectra of graphitic carbon in pyroxene. j) Representative Raman spectra for the figure. Pyx – pyroxene, Act – actinolite, Qtz – quartz. Raman map colours: grey – orthopyroxene, orange – actinolite, blue – quartz, green – calcite, yellow – magnetite, purple – poorly crystalline graphite, red – crystalline graphite.

multiple crystallinities of disordered organic carbon have been found co-occurring in chert from the Apex Formation (Marshall et al., 2012) in Western Australia, and with graphite in greenschist and amphibolite grade pelitic rocks (Kribek et al., 2008; Large et al., 1994). Varying crystallinity of graphitic carbon in metamorphic terranes may be due to the preservation of fluid-deposited graphite along with syngenetic graphite (Crespo et al., 2004), or varying temperature and H_2 fugacity of C–O–H fluids during deposition of graphite (Pasteris and Chou, 1998).

Graphite and PCG in the Nuvvuagittuq, Anshan and Wutai BIF, therefore, have one of two possible mechanisms of formation: 1) the graphite was formed from metamorphism of organic matter deposited in the sedimentary rocks and PCG precipitated from C–O–H fluids (Crespo et al., 2005), or 2) all graphitic carbon was precipitated from C–O–H fluids, of varying temperature or H_2 fugacity, which precipitated carbon (Pasteris and Chou, 1998) with varying crystallinities. In the Nuvvuagittuq BIF, PCG veins (Fig. 1) contain only PCG, and not graphite, suggesting there was just one generation of fluid-deposited graphite. Additionally, crystalline graphite does not appear with retrograde minerals, which suggests that only PCG was fluid-deposited. Low temperatures are required for PCG precipitation from C–O–H, so that fluid-deposited PCG is relatively uncommon in nature due to the high solubility of carbon at low temperatures (Luque and Rodas, 1999;

Pasteris, 1999). The low fO_2 and high CH_4 content of carbonic fluids generated at low pressures and temperatures (French, 1966) from the maturation of organic matter encourage precipitation of disordered graphite, where it would otherwise be unstable in typically more oxidised crustal carbonic fluids (Pasteris, 1999). Low-temperature carbonic fluids are close to graphite saturation and precipitate graphite they move, rather than transporting carbon long distances. This may be due to the low temperature of the fluids, making them susceptible to abrupt changes in pressure–temperature (Pasteris, 1999). Much of this graphite may nucleate on pre-existing graphite, thereby making carbon unavailable for widespread deposition (Crespo et al., 2004; Pasteris, 1999).

The distances of carbon transport in the Nuvvuagittuq appear to have ranged from a few microns to perhaps centimetres, as evidenced by PCG within micron-sized veins cutting across thin sections (Fig. 1). This is in contrast to high temperature graphite deposits, which transfer carbon over long distances in the crust, from 10 s of metres to possibly kilometres (Luque et al., 2014). Since there are no reported graphite veins cross-cutting the Nuvvuagittuq belt, graphite was likely not widely mobile. The association of crystalline graphite and PCG, together with the lack of widely distributed graphite veins, (over 10 s of metres to kilometres) is consistent with a localised source of carbon. Therefore, PCG in the Nuvvuagittuq, Anshan and Wutai BIF (Fig. 3a–d; 5d–h; 6a–f) was
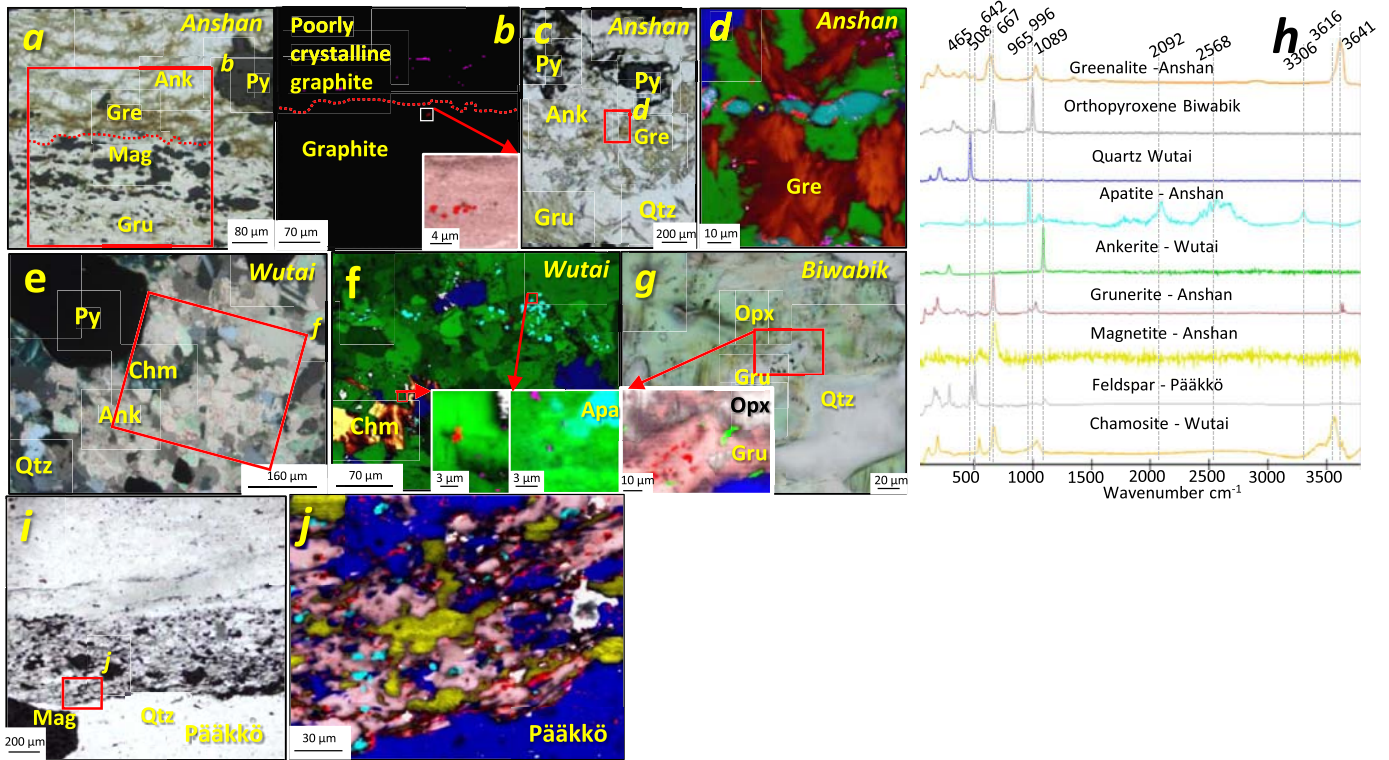
Fig. 6. Graphitic carbon in strongly metamorphosed BIFs. a) PPL image of grunerite and magnetite layers in the Anshan BIF. b) Graphite filter map showing the localised occurrences of PCG and graphite. c) PPL image of grunerite and pyrite layer in the Anshan BIF. d) Raman map of apatite with coatings of graphite, along with surrounding PCG and greenalite. e) CP image of ankerite and pyrite layer in the Wutai BIF. f) Raman showing the close association of PCG and graphite and PCG with apatite. g) PPL image of clinopyroxene exhibiting grunerite rims with inclusions of graphitic carbon in the Biwabik BIF. h) Raman spectra for this figure. i) PPL image of grunerite–magnetite layer in the Pääkkö BIF. j) Raman map showing the association of graphite with apatite and grunerite. Mineral abbreviations: Ank – ankerite, Gru – grunerite, Py – pyrite, Chm – chamosite. Raman map colours: grey – orthopyroxene (Biwabik)/feldspar (Pääkkö), orange – greenalite (Anshan)/chamosite (Wutai), brown – grunerite, blue – quartz, turquoise – apatite, green – ankerite, yellow – magnetite, purple – poorly crystalline graphite, red – crystalline graphite. See Fig. 3 for graphite spectra.
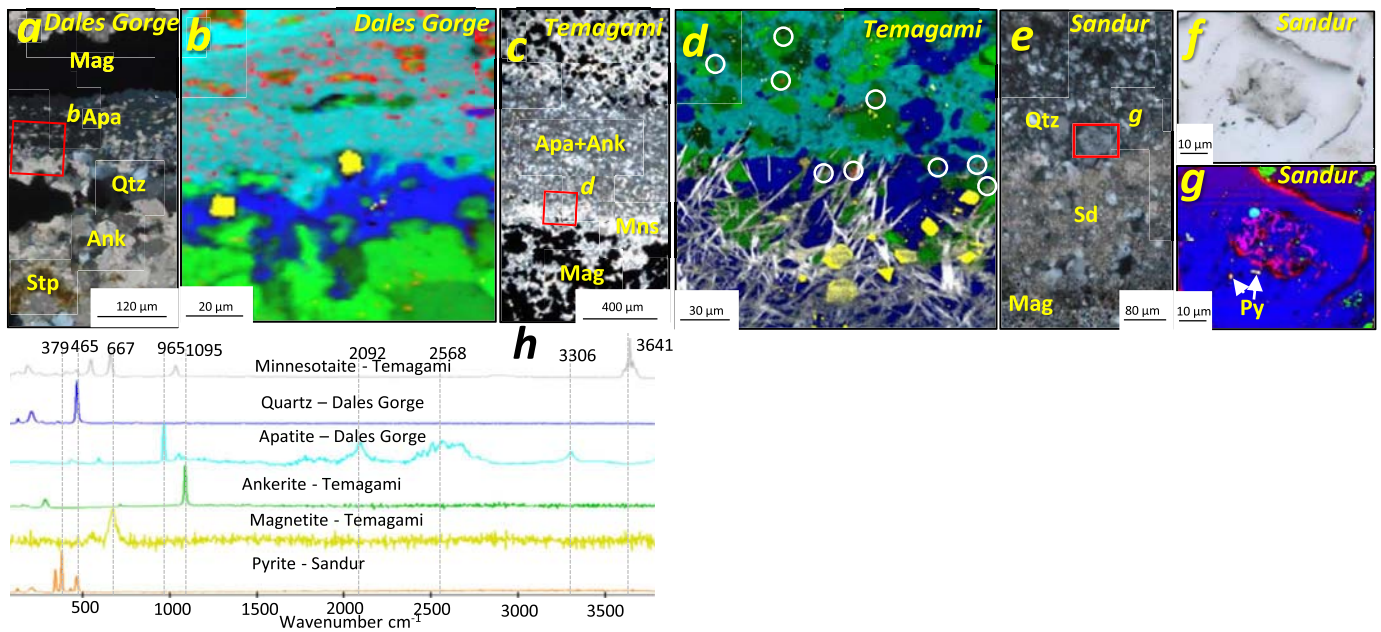
Fig. 7. Graphitic carbon and apatite in weakly metamorphosed BIFs. a) CP image of magnetite and apatite bands in the Dales Gorge BIF, box corresponds to b. b) Raman map of graphitic carbon in apatite. c) CP image of apatite band with ankerite in the Temagami BIF, box corresponds to d. d) Raman map of apatite band with ankerite and graphitic carbon inclusions (circled). e) CP image of siderite and magnetite band in the Sandur BIF, box corresponds to f. f) PPL image of inclusions in quartz. g) Raman map of graphite and PCG associated with apatite and pyrite. h) Raman spectra for this figure. Raman map colours: grey – minnesotaite, orange – pyrite, blue – quartz, turquoise – apatite, green – ankerite, yellow – magnetite, purple – poorly crystalline graphite, red – crystalline graphite. See Fig. 3 for graphite spectra.

Table 2
Stable isotope compositions of OM and carbonate in bulk rock powders of BIFs in this study.

Sample name	TOC (%)	$\delta^{13}C_{org}$ (VPDB) (‰)	$\delta^{13}C_{Carb}$ (VPBD) (‰)	$\delta^{18}O_{Carb}$ (SMOW) (‰)
G91-26C Akilia[a]	0.01	−17.5	−4.4	+14.0
PC0814 (NSB)	0.03	−28.1	bdl	bdl
PC0825 (NSB)	0.05	−26.4	−7.0	+18.5
PC-075 (NSB)	bdl	bdl	−4.9	+15.5
PC-014 (NSB)	bdl	bdl	bdl	bdl
PC-091 (NSB)	bdl	bdl	−4.5	+16.5
BIFs-8 (Sandur)	0.21[b]	−28.5	−9.5	+17.3
TE0704 (Temagami)	0.04	−27.8	−4.6	+15.7
ANS0911 (Anshan)	0.03	−22.0	−7.3	+14.5
ANS0917 (Anshan)	0.03	−26.7	−8.2	+14.5
WUT1512 (Wutai)	0.05	−22.5	−3.4	+10.5
DGM-1-198-6 (Dales Gorge)	0.03	−25.2	−10.3	+19.9
MF-62-88 (Biwabik)	0.03	−28.4	bdl	bdl
PK344-156.4 (Pääkkö)	0.45	−19.6	−3.7	+21.0

[a] Denotes data taken from Papineau et al. (2010b). bdl – below detection limit.
[b] Organic and acid insoluble mineral extract. Samples weighed between 30–60 mg for organic analyses.

likely partly sourced *in-situ*, and precipitated within centimetres of the source, from low fO_2 and high CH_4 carbonic fluids. The occurrence of PCG on the rims of crystalline graphite in isolated orthopyroxene crystals is unlikely to arise from infiltration of external $H_2O + CO_2 + CH_4$ fluids, without leaving nearby trails of PCG, which are not seen in Raman or optical images (Fig. 5). This observation is consistent with localised $H_2O + CO_2 + CH_4$ fluids being partially sourced *in-situ* from syngenetic organics (now crystalline graphite). Though it is not possible to fully exclude an external source for some of the carbon in the C–O–H fluids, it is concluded that PCG in the Nuvvuagittuq BIF precipitated from cooling carbon-bearing fluids derived from devolatilisation reactions, which liberated CO_2 and CH_4 from pre-existing organic matter (now graphite) and precipitated it as PCG. A detailed comparative assessment with all known incidences of graphitic carbon with apatite in BIF (Supplementary Table 3), shows that PCG in other BIF may also represent devolatilised and remobilised organic material. The origins of this organic matter, however, need to be assessed on an individual basis.

3.5. Sources of carbon in graphite and testing the null hypothesis

Discounting younger rocks rich in organic matter by their absence from the Nuvvuagittuq area, the source of carbon in carbon-bearing fluids in the BIF has three possible origins: 1) mantle or sub-lithospheric CO_2 and CH_4, 2) decarbonation of carbonates and 3) devolatilisation of syngenetic organic matter (Luque et al., 2014). The graphitic carbon in the greenschist facies Brockman, Temagami, Sandur and Wutai BIF have $\delta^{13}C_{gra}$ values of −25.2‰, −27.8‰, −28.5‰, and −22.5‰ respectively. While in the amphibolite facies Pääkkö, Nuvvuagittuq and Anshan BIF, $\delta^{13}C_{gra}$ values are −19.6‰, −28.1‰ to −26.4‰, and −26.7 to −22.0‰ respectively. In the hornfels–pyroxene facies Biwabik and granulite facies Akilia BIF, the bulk rock $\delta^{13}C_{gra}$ values are, −28.1‰ and −17.5‰, respectively (Table 2). All these values fall within the average composition of sedimentary organic matter over the last 3,500 Myr (Schidlowski, 2001), except the Akilia bulk $\delta^{13}C_{gra}$ values, yet *in-situ* analyses on individual graphite coatings on apatite grains have a very large range between −4 and −49‰ (McKeegan et al., 2007; Mojzsis et al., 1996; Papineau et al., 2010b), which is consistent with a protracted metamorphic history. Decarbonation reactions can be ruled out, as the $\delta^{13}C_{carb}$ values for all the BIF are sig-

nificantly heavier (−4.4 and −9.1‰) than $\delta^{13}C_{gra}$ values (Table 2) (Papineau et al., 2011). Additionally, Rayleigh distillation effects would only shift C isotopes toward heavier compositions (Luque et al., 2012) during precipitation of C from C–O–H fluids. Conversely, during retrograde reactions fluid compositions with CO_2 > CH_4, may shift C isotopes of precipitated graphite to lighter values (Farquhar et al., 1999). However, under typical crustal conditions, fluids are reducing and CH_4 dominates (Eiler et al., 1997). This may be especially true of BIF, which typically contain reduced mineral assemblages such as magnetite, so that, CO_2 concentrations are unlikely to have been greater than CH_4, ruling out a retrograde reaction as the origin of light C isotope compositions. Fluid-deposited graphite derived from C–O–H fluids of mantle origin are typically much heavier than −14‰ (Luque et al., 1998; Pearson et al., 1994). Moreover, we argue that meteoritic organic matter can be ruled out due to the absence of detrital or meteorite components in the BIF sediments, expected to be deposited along with meteoritic organic matter.

The production of abiotic organic matter in hydrothermal vents is known to produce isotopically light hydrocarbons, typically with less than four carbon atoms (Charlou et al., 2010; McCollom, 2013; McCollom and Seewald, 2007). The isotopic signature of these hydrocarbons are characteristically not lighter than −15 to −19‰ in natural vent sites (McDermott et al., 2015; Proskurowski et al., 2008). Yet, experimental reduction of inorganic carbon compounds such as CO, CO_2 and HCO_3^- has yielded CH_4 with isotopic compositions reaching as low as −50‰ (Horita and Berndt, 1999; McCollom and Seewald, 2007). If during metamorphism isotopically light CH_4 was produced by reduction of CO_2 in the Nuvvuagittuq or other BIF, CO_2 would also react with the CH_4 produced in order to precipitate graphite (Equ. (1)). Therefore, the bulk isotopic composition of graphitic carbon in the Nuvvuagittuq BIF is equivalent to the original CO_2 reservoir of a closed system. Bulk rock powders can be used to roughly estimate the isotopic composition of crystalline graphite and PCG in the Nuvvuagittuq BIF. For example, the Nuvvuagittuq jasper-carbonate BIF samples only contain crystalline graphite (PC0822, PC0844)(Dodd et al., 2017) and have $\delta^{13}C_{org}$ values of −21.1 to −24.6‰, whereas the Nuvvuagittuq silicate BIF samples contain predominately PCG and have a similar range of $\delta^{13}C_{org}$ values of −20.6 to −26.4‰ (PC0825, Fig. 1) (Papineau et al., 2011). Further *in-situ* work is needed to precisely determine their individual carbon isotopic compositions. If these estimates for the isotopic compositions of PCG and crystalline graphite are correct, their similar isotopic composition is an expected result from liberation of CO_2 and CH_4 from a common syngenetic source of organic matter, and precipitation via equation (1) (Crespo et al., 2004). In other words, a significant amount of retrograde PCG was likely sourced from syngenetic organic matter, and this syngenetic organic matter now occurs as crystalline graphite formed during prograde metamorphism.

To further test for possible non-biological sources of organic matter (now preserved as crystalline graphite), we consider abiotic hydrocarbon synthesis in serpentinites from the Nuvvuagittuq belt. Serpentinites from the Nuvvuagittuq belt occur in ultramafic rocks, which are interpreted to be co-genetic with the Ujaraaluk amphibolite (O'Neil et al., 2011). The composition of the Ujaraaluk amphibolite, along with the association of anthophyllite-cordierite Mg-rich rocks, is consistent with hydrothermal alteration of oceanic crust (O'Neil et al., 2011), likely responsible for the serpentinisation. Deposition of the BIF is believed to be associated with this hydrothermal activity on the seafloor. Moreover, the BIF is found between the layers of serpentinite in the belt (O'Neil et al., 2011). Pentlandite [(Fe, Ni, Co)$_9$S$_8$] (Supplementary Table 1) is a common mineral in these serpentinites, and believed to be an effective natural catalyst of Fischer–Tropsch reactions in natural settings (Horita and Berndt, 1999; McCollom, 2013). However,
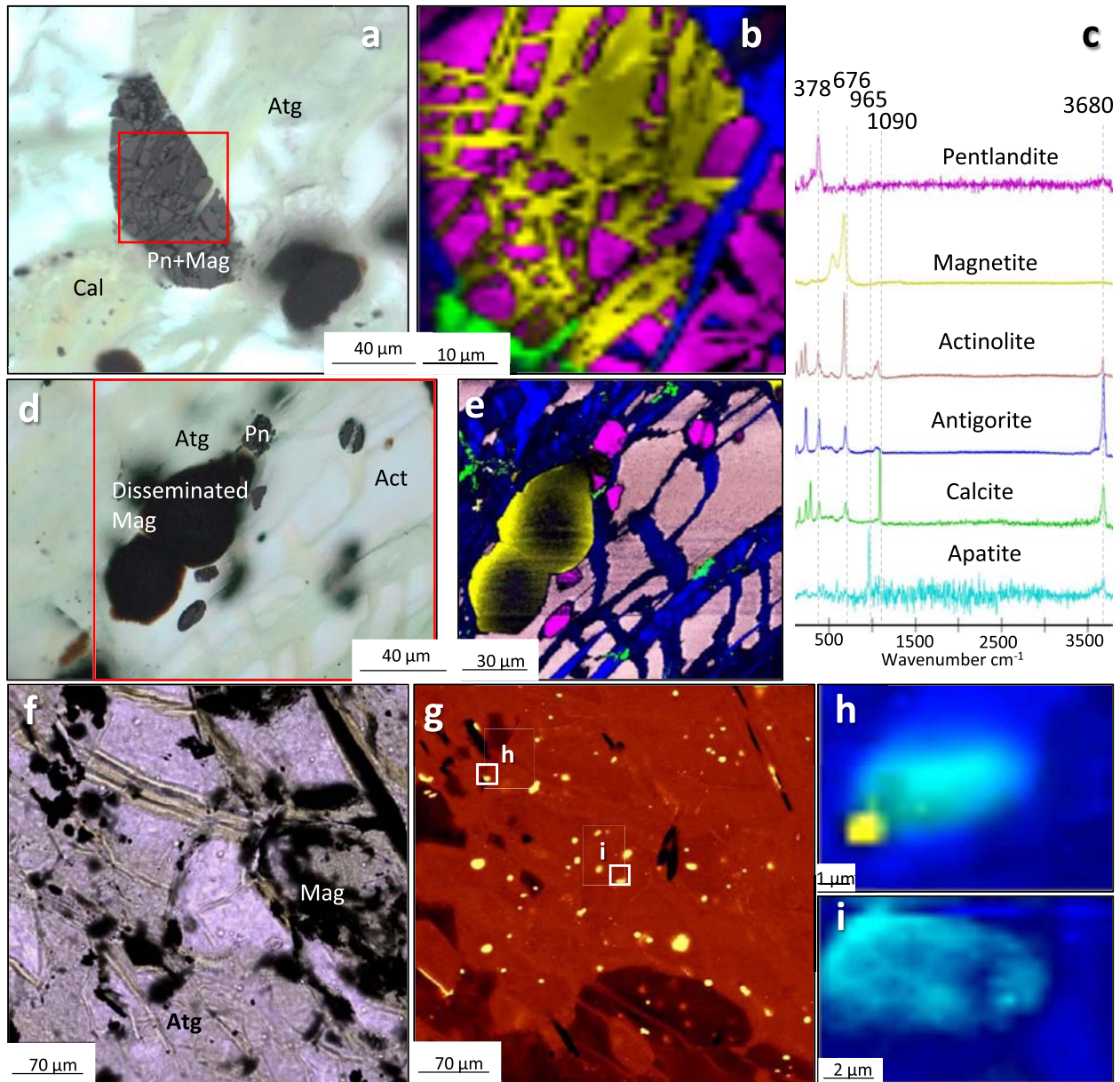
Fig. 8. Selected targets from serpentinite rocks associated with the Nuvvuagittuq BIF, PC-075. a) PPL image of pentlandite–magnetite crystal in a matrix of antigorite and carbonate. b) Raman map of pentlandite and magnetite grain with calcite. c) Representative Raman spectra for this figure. d) PPL image of magnetite associated with pentlandite in serpentinite. e) Raman map pentlandite and magnetite grains show no association with reduced carbon in the presence of calcite. f) PPL image of serpentinite with magnetite and apatite crystals. g) Raman map for filter 965 cm^{-1} shows apatite distribution, boxes correspond to h–i. h–i) Raman map of apatite from panel e show no graphitic carbon associations. Pn – pentlandite, Atg – antigorite, Cal – calcite, Mag- magnetite. Raman map colours: brown – actinolite, blue – quartz, turquoise – apatite, green – calcite, yellow – magnetite, purple – pentlandite.

among twenty-five Raman scans over three samples, we found no organic matter associated with these minerals, nor did we find organic carbon associated with apatite and carbonate in the serpentinite (Fig. 8). To corroborate these observations, results from the analysis of bulk rock powders of the serpentinite showed no detectable organic matter (Table 2).

The serpentinites contain all the necessary ingredients for organic synthesis, including suitable catalysts (pentlandite) and a carbon source (carbonate), yet organic matter was not detected. While the analyses of three serpentinite samples is not exhaustive, as it currently stands these new observations suggest that abiotic hydrocarbon production during serpentinisation in seafloor systems was unlikely to be significant during deposition of the Nuvvuagittuq BIF. Alternatively, abiotic organic matter may not be retained in serpentinites. The restricted range of C isotopic compositions of graphitic carbon in BIF throughout the Precambrian suggests a similar C-isotope fractionation process, which is likely a biological one. We acknowledge that while modern hydrothermal vents produce abiotic organics with δ^{13}C signatures higher than that of the reported graphitic carbons, Archean hydrothermal systems may have synthesised organics with lower δ^{13}C signatures, as inferred by experiments (Horita and Berndt, 1999). Finally, the possibility of some ^{13}C-depleted CO_2 or CH_4 infiltration into the rock during metamorphism cannot be fully excluded, but coatings of PCG on crystalline graphite, as well as similar isotopic compositions between BIF samples (Papineau et al., 2011), point to an *in-situ*, syngenetic, and sedimentary source of carbon.

4. Implications and conclusions

The occurrence of ^{13}C-depleted graphite associations with apatite in one of Earth's oldest BIF, and its use as a biosignature, has been a subject of controversy (Lepland et al., 2005; McKeegan et al., 2007; Mojzsis et al., 1996; Nutman and Friend, 2006). Several studies failed to find apatite + graphite mineral assemblages in the Akilia BIF, or presumed such associations to be rare (Lepland et al., 2005; Nutman and Friend, 2006). Subsequently it was found that about 25% of apatite grains were associated with graphite (Papineau et al., 2010a). The documentation of 10 different BIF, from the Eoarchaean to the Palaeoproterozoic, show the mineral association of apatite + graphite to be commonplace in BIF across various metamorphic grades. However, we did not find evidence for graphite inclusions in apatite, as previous studies have claimed (McKeegan et al., 2007; Mojzsis et al., 1996), with graphite frequently coating apatite. Graphite particles which occur in the centre of apatite grains (Fig. 3d) may be coatings in the line of sight (Papineau et al., 2010a). Yet large apatite bands in the Dales gorge BIF appear to have inclusions of kerogen (Fig. 7b), so graphite inclusions in apatite remain possible.

Apatite and graphite mineral assemblages in BIF are viewed here as having two possible origins. In greenschist facies BIF, graphitic carbon is found in sedimentary bands of carbonate and apatite. These likely represent the mineralised products of decayed biological organic matter (Li et al., 2011), as observed in the Brockman, Temagami and Sandur BIF. These mineral associations persist into the amphibolite facies, where graphite is associated with apatite, in the Pääkkö, Anshan, and Saglek BIF (Fig. 3j–l; 6d, j). Furthermore, the occurrence of apatite and graphite from the 3,780 to 3,920 Myr Saglek BIF could provide support for previous interpretations that graphite with ^{13}C-depleted isotopic compositions from the Saglek belt represents microbial remains (Tashiro et al., 2017).

In highly metamorphosed BIF, higher temperatures may lead to cracking of kerogen, which produces significant quantities of CH$_4$. The association of PCG with retrograde minerals points to the fluid-deposition of apatite and PCG during retrograde metamorphism, a process that can proceed at the upper greenschist to amphibolite facies, for instance in the Anshan, Biwabik, Akilia and Nuvvuagittuq BIF (Supplementary Table 3). The fluid deposition of apatite during metamorphism may be supported by other studies which found the rare-earth element patterns of apatite from the Akilia and other Eoarchaean BIF to be consistent with a metamorphic origin (Lepland et al., 2002; Nutman and Friend, 2006). While graphitic carbon associated with apatite is commonplace in Eoarchaean to Palaeoproterozoic BIF, the possibility of their co-precipitation during metamorphism means that the null hypothesis for a biological source of carbon in graphite cannot be fully rejected. This is based on experiments that show that non-biological C-isotope fractionation overlaps the biological range, and that carbon in C–O–H fluids may include several different sources. From the detailed study of variably aged and metamorphosed BIFs, uniformitarianism suggests apatite + graphite biosignatures in Earth's oldest rocks are ambiguous indicators of life, unless they can be proven to be syngenetic and shown to be associated with other possible biosignatures, such as in the case of the Nuvvuagittuq jasper-carbonate BIF (Dodd et al., 2017). In this instance the crystalline structure of the graphite is consistent with a syngenetic origin, unlike PCG (Fig. 4; Supplementary Fig. 1), and the apatite in which it sometimes occurs forms large euhedral laths, consistent with prograde apatite (Nutman, 2007). Therefore, in this case the apatite + graphite + carbonate association fits best with an origin from biomass remineralisation, as can be inferred for the Dales gorge BIF and those younger.

The new results presented here show fluid-deposited graphite is commonly associated with apatite in Earth's oldest sedimentary rocks, and therefore evidence for life's emergence on Earth rests in part on the identification of fluid-deposited and syngenetic graphite. The work here suggests that fluid-deposited carbon is partly sourced from syngenetic organic matter, the origin of which could either be pre-biotic or the remains of Earth's first lifeforms.

Appendix A. Supplementary material

Supplementary material related to this article can be found online at https://doi.org/10.1016/j.epsl.2019.01.054.

References

Arita, Y., Wada, H., 1990. Stable isotopic evidence for migration of metamorphic fluids along grain boundaries of marbles. Geochem. J. 24 (3), 173–186.

Beyssac, O., Goffe, B., Chopin, C., Rouzaud, J.N., 2002. Raman spectra of carbonaceous material in metasediments: a new geothermometer. J. Metamorph. Geol. 20, 859–871.

Beyssac, O., Goffé, B., Petitet, J.-P., Froigneux, E., Moreau, M., Rouzaud, J.-N., 2003. On the characterization of disordered and heterogeneous carbonaceous materials by Raman spectroscopy. Spectrochim. Acta, Part A, Mol. Biomol. Spectrosc. 59 (10), 2267–2276.

Charlou, J.L., Donval, J.P., Konn, C., Ondréas, H., Fouquet, Y., 2010. High production and fluxes of H$_2$ and CH$_4$ and evidence of abiotic hydrocarbon synthesis by serpentinization in ultramafic-hosted hydrothermal systems on the Mid-Atlantic Ridge. In: Rona, Peter A., Jérôme Dyment, C.W.D., Murton, Bramley J. (Eds.), Diversity of Hydrothermal Systems on Slow Spreading Ocean Ridges. American Geophysical Union, Washington, D.C., pp. 265–296.

Crespo, E., Luque, F.J., Barrenechea, J.F., Rodas, M., 2005. Mechanical graphite transport in fault zones and the formation of graphite veins. Mineral. Mag. 69 (4), 463–470.

Crespo, E., Luque, J., FernÁNdez-RodríGuez, C., Rodas, M., DíAz-Azpiroz, M., FernÁNdez-Caliani, J.C., Barrenechea, J.F., 2004. Significance of graphite occurrences in the Aracena Metamorphic Belt, Iberian Massif. Geol. Mag. 141 (6), 687–697.

Dodd, M.S., Papineau, D., Grenne, T., Slack, J.F., Rittner, M., Pirajno, F., O'Neil, J., Little, C.T.S., 2017. Evidence for early life in Earth's oldest hydrothermal vent precipitates. Nature 543 (7643), 60–64.

Dodd, M.S., Papineau, D., She, Z., Fogel, M.L., Nederbragt, S., Pirajno, F., 2018. Organic remains in late Palaeoproterozoic granular iron formations and implications for the origin of granules. Precambrian Res. 310, 133–152.

Eiler, J.M., Mojzsis, S.J., Arrhenius, G., 1997. Carbon isotope evidence for early life. Nature 386, 665.

Farquhar, J., Hauri, E., Wang, J., 1999. New insights into carbon fluid chemistry and graphite precipitation: SIMS analysis of granulite facies graphite from Ponmudi, South India. Earth Planet. Sci. Lett. 171 (4), 607–621.

French, B.M., 1966. Some geological implications of equilibrium between graphite and a C–H–O gas phase at high temperatures and pressures. Rev. Geophys. 4 (2), 223–253.

Gaillard, N., Williams-Jones, A.E., Clark, J.R., Lypaczewski, P., Salvi, S., Perrouty, S., Piette-Lauzière, N., Guilmette, C., Linnen, R.L., 2018. Mica composition as a vector to gold mineralization: deciphering hydrothermal and metamorphic effects in the Malartic district, Quebec. Ore Geol. Rev. 95, 789–820.

Horita, J., Berndt, M.E., 1999. Abiogenic methane formation and isotopic fractionation under hydrothermal conditions. Science 285, 1055–1057.

Klein, C., 2005. Some Precambrian banded iron-formations (BIFs) from around the world: their age, geologic setting, mineralogy, metamorphism, geochemistry, and origins. Am. Mineral. 90 (10), 1473–1499.

Kribek, B., Sykorova, I., Machovic, V., Laufek, F., 2008. Graphitization of organic matter and fluid-deposited graphite in Palaeoproterozoic (Birimian) black shales of the Kaya–Goren greenstone belt (Burkina Faso, West Africa). J. Metamorph. Geol. 26 (9), 937–958.

Large, D.J., Christy, A.G., Fallick, A.E., 1994. Poorly crystalline carbonaceous matter in high grade metasediments: implications for graphitisation and metamorphic fluid compositions. Contrib. Mineral. Petrol. 116, 108–116.

Lepland, A., Arrhenius, G., Cornell, D., 2002. Apatite in early Archean Isua supracrustal rocks, southern West Greenland: its origin, association with graphite and potential as a biomarker. Precambrian Res. 118, 221–241.

Lepland, A., van Zuilen, M.A., Arrhenius, G., Whitehouse, M.J., Fedo, C.M., 2005. Questioning the evidence for Earth's earliest life – Akilia revisited. Geology 33 (1), 77.

Lepland, A., van Zuilen, M.A., Philippot, P., 2011. Fluid-deposited graphite and its geobiological implications in early Archean gneiss from Akilia, Greenland. Geobiology 9 (1), 2–9.

Li, Y.L., Konhauser, K.O., Cole, D.R., Phelps, T.J., 2011. Mineral ecophysiological data provide growing evidence for microbial activity in banded-iron formations. Geology 39 (8), 707–710.

Li, Y.L., Sun, S., Chan, L.S., 2012. Phosphogenesis in the 2460 and 2728 million-year-old banded iron formations as evidence for biological cycling of phosphate in the early biosphere. Evol. Ecol. 3 (1), 115–125.

Luque, F.J., Crespo-Feo, E., Barrenechea, J.F., Ortega, L., 2012. Carbon isotopes of graphite: implications on fluid history. Geosci. Front. 3 (2), 197–207.

Luque, F.J., Huizenga, J.M., Crespo-Feo, E., Wada, H., Ortega, L., Barrenechea, J.F., 2014. Vein graphite deposits: geological settings, origin, and economic significance. Miner. Depos. 49 (2), 261–277.

Luque, F.J., Pasteris, J.D., Wopenka, B., Rodas, M., Barrenechea, J.F., 1998. Natural fluid-deposited graphite: mineralogical characteristics and mechanisms of formation. Am. J. Sci. 298, 471–498.

Luque, F.J., Rodas, M., 1999. Constraints on graphite crystallinity in some Spanish fluid-deposited occurrences from different geologic settings. Miner. Depos. 34, 215–219.

Marshall, A.O., Emry, J.R., Marshall, C.P., 2012. Multiple generations of carbon in the apex chert and implications for preservation of microfossils. Astrobiology 12 (2), 160–166.

McCollom, T.M., 2013. Laboratory simulations of abiotic hydrocarbon formation in Earth's deep subsurface. In: Hazen, R.M., Jones, A.P., Baross, J.A. (Eds.), Carbon in Earth, vol. 75. Virginia Mineralogical Society of America, pp. 467–490.

McCollom, T.M., Seewald, J.S., 2007. Abiotic synthesis of organic compounds in deep-sea hydrothermal environments. Chem. Rev. 107 (2), 382–401.

McDermott, J.M., Seewald, J.S., German, C.R., Sylva, S.P., 2015. Pathways for abiotic organic synthesis at submarine hydrothermal fields. Proc. Natl. Acad. Sci. USA 112 (25), 7668–7672.

McKeegan, K.D., Kudryavtsev, A.B., Schopf, J.W., 2007. Raman and ion microscopic imagery of graphitic inclusions in apatite from older than 3830 Ma Akilia supracrustal rocks, west Greenland. Geology 35 (7), 591.

Mojzsis, S.J., Arrhenius, G., McKeegan, K.D., Harrison, T.M., Nutman, A.P., Friend, C.R.L., 1996. Evidence for life on Earth before 3,800 million years ago. Nature 384, 55–59.

Nutman, A.P., 2007. Apatite recrystallisation during prograde metamorphism, Cooma, southeast Australia: implications for using an apatite – graphite association as a biotracer in ancient metasedimentary rocks. Aust. J. Earth Sci. 54 (8), 1023–1032.

Nutman, A.P., Friend, C.R.L., 2006. Petrography and geochemistry of apatites in banded iron formation, Akilia, W. Greenland: consequences for oldest life evidence. Precambrian Res. 147 (1–2), 100–106.

O'Neil, J., Francis, D., Carlson, R.W., 2011. Implications of the Nuvvuagittuq greenstone belt for the formation of Earth's early crust. J. Petrol. 52 (5), 985–1009.

Papineau, D., De Gregorio, B.T., Cody, G.D., Fries, M.D., Mojzsis, S.J., Steele, A., Stroud, R.M., Fogel, M.L., 2010a. Ancient graphite in the Eoarchean quartz–pyroxene rocks from Akilia in southern West Greenland, I: petrographic and spectroscopic characterization. Geochim. Cosmochim. Acta 74 (20), 5862–5883.

Papineau, D., De Gregorio, B.T., Stroud, R.M., Steele, A., Pecoits, E., Konhauser, K., Wang, J., Fogel, M.L., 2010b. Ancient graphite in the Eoarchean quartz–pyroxene rocks from Akilia in southern West Greenland, II: isotopic and chemical compositions and comparison with Paleoproterozoic banded iron formations. Geochim. Cosmochim. Acta 74 (20), 5884–5905.

Papineau, D., De Gregorio, B.T., Cody, G.D., O'Neil, J., Steele, A., Stroud, R.M., Fogel, M.L., 2011. Young poorly crystalline graphite in the >3.8-Gyr-old Nuvvuagittuq banded iron formation. Nat. Geosci. 4 (6), 376–379.

Papineau, D., De Gregorio, B., Fearn, S., Kilcoyne, D., McMahon, G., Purohit, R., Fogel, M., 2016. Nanoscale petrographic and geochemical insights on the origin of the Palaeoproterozoic stromatolitic phosphorites from Aravalli Supergroup, India. Geobiology 14 (1), 3–32.

Pasteris, J.D., 1999. Causes of the uniformly high crystallinity of graphite in large epigenetic deposits. J. Metamorph. Geol. 17, 779–787.

Pasteris, J.D., Chou, I.-M., 1998. Fluid-deposited graphitic inclusions in quartz: comparison between KTB (German Continental Deep-Drilling) core samples and artificially reequilibrated natural inclusions. Geochim. Cosmochim. Acta 62 (1), 109–122.

Pearson, D.G., Boyd, F.R., Haggerty, S.E., Pasteris, J.D., Field, S.W., Nixon, P.H., Pokhilenko, N.P., 1994. The characterisation and origin of graphite in cratonic lithospheric mantle: a petrological carbon isotope and Raman spectroscopic study. Contrib. Mineral. Petrol. 115, 449–466.

Proskurowski, G., Lilley, M.D., Seewald, J.S., Früh-Green, G.L., Olson, E.J., Lupton, J.E., Sylva, S.P., Kelley, D.S., 2008. Abiogenic hydrocarbon production at Lost City hydrothermal field. Science 319, 604–607.

Satish-Kumar, M., Jaszczak John, A., Hamamatsu, T., Wada, H., 2011. Relationship between structure, morphology, and carbon isotopic composition of graphite in marbles: implications for calcite–graphite carbon isotope thermometry. Am. Mineral. 96, 470.

Schidlowski, M., 2001. Carbon isotopes as biogeochemical recorders of life over 3.8 Ga of Earth history: evolution of a concept. Geochim. Cosmochim. Acta 106, 117–134.

She, Z.-B., Strother, P., Papineau, D., 2014. Terminal Proterozoic cyanobacterial blooms and phosphogenesis documented by the Doushantuo granular phosphorites, II: microbial diversity and C isotopes. Precambrian Res. 251, 62–79.

Tashiro, T., Ishida, A., Hori, M., Igisu, M., Koike, M., Mejean, P., Takahata, N., Sano, Y., Komiya, T., 2017. Early trace of life from 3.95 Ga sedimentary rocks in Labrador, Canada. Nature 549 (7673), 516–518.

Valley, J.W., O'Neil, J.R., 1981. ^{13}C^{12}C exchange between calcite and graphite: a possible thermometer in Grenville marbles. Geochim. Cosmochim. Acta 45 (3), 411–419.

van Zuilen, M.A., Fliegel, D., Wirth, R., Lepland, A., Qu, Y., Schreiber, A., Romashkin, A.E., Philippot, P., 2012. Mineral-templated growth of natural graphite films. Geochim. Cosmochim. Acta 83, 252–262.

Wang, A., Dhamenincourt, P., Dubessy, J., Guerard, D., Landais, P., Lelaurain, M., 1989. Characterization of graphite alteration in an uranium deposit by micro-Raman spectroscopy, X-ray diffraction, transmission electron microscopy and scanning electron microscopy. Carbon 27 (2), 209–218.